PNAS
www.pnas.org

Supplementary Information for

Structural basis for DEAH-helicase activation by G-patch proteins

Michael K. Studer, Lazar Ivanović, Marco E. Weber, Sabrina Marti, Stefanie Jonas

Correspondence should be addressed to:
Stefanie Jonas
Institute of Molecular Biology and Biophysics, ETH Zurich
Otto-Stern-Weg 5
CH-8093 Zurich, Switzerland
Phone: +41-44-63-30722
Fax: +41-44-63-31294
stefanie.jonas@mol.biol.ethz.ch

This PDF file includes:

Figures S1 to S7
Table S1
SI References

www.pnas.org/cgi/doi/10.1073/pnas.1913880117

Studer et al. Supplemental Figure 1

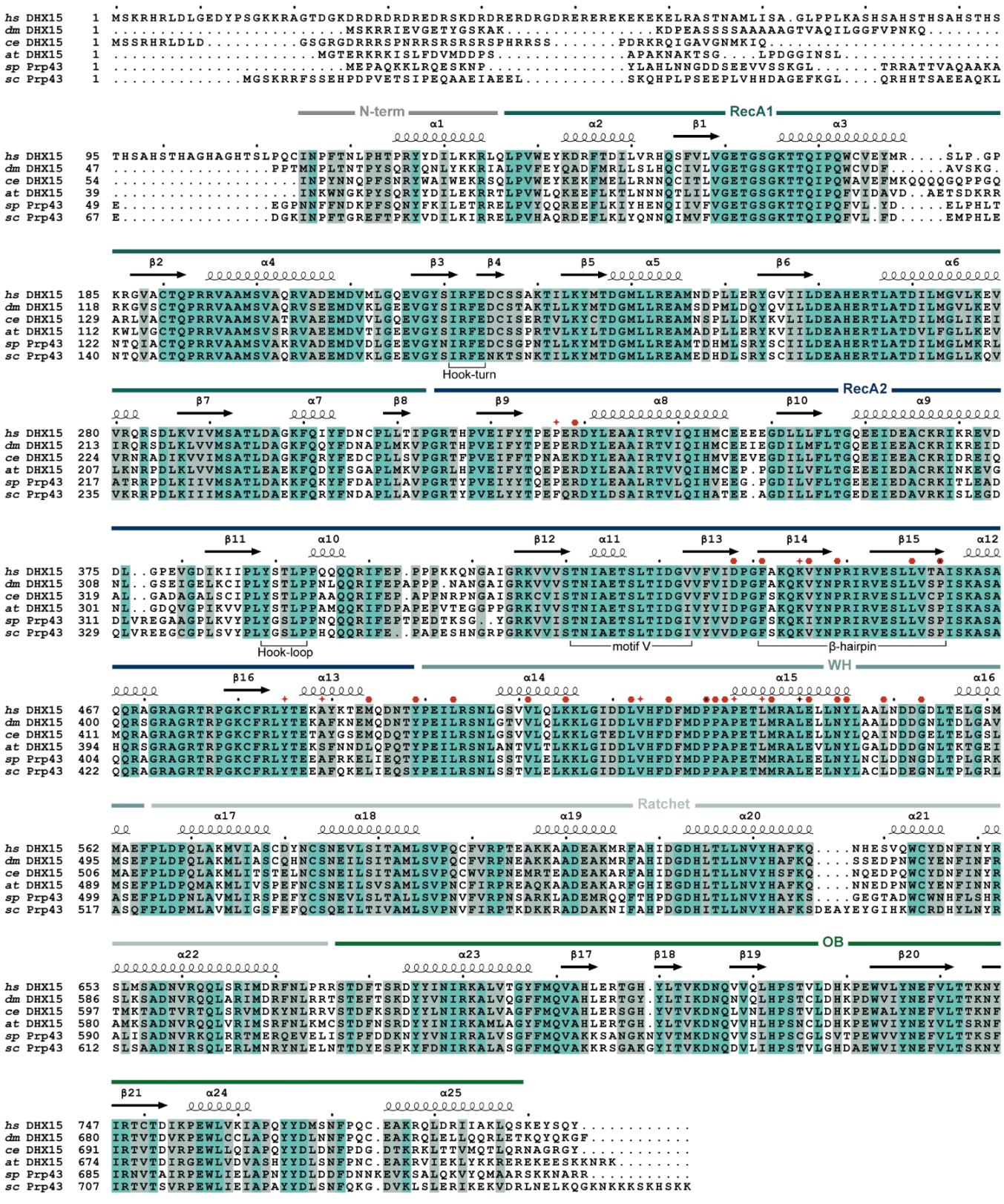

Fig. S1. The G-patch interface is highly conserved amongst DHX15/Prp43 orthologs.

Sequence alignment of eukaryotic DHX15/Prp43 orthologs from *Homo sapiens* (*hs*), *Drosophila melanogaster* (*dm*), *Caenorhabditis elegans* (*ce*), *Arabidopsis thaliana* (*at*), *Schizosaccharomyces pombe* (*sp*), *Saccharomyces cerevisiae* (*sc*). Residues with complete conservation or 70% similarity are highlighted in petrol and grey, respectively. Secondary structure elements as observed in the *hs*DHX15-G-patch complex structure are denoted above the alignment. Red hexagons mark amino acids that are part of the G-patch interface, while red stars indicate residues that were mutated in this study. *hs*DHX15 domains that are present in the current structure are marked above the alignment and colored as in Fig. 1. Motifs that are relevant for RNA binding are labelled below the sequences.

Studer et al. Supplemental Figure 2

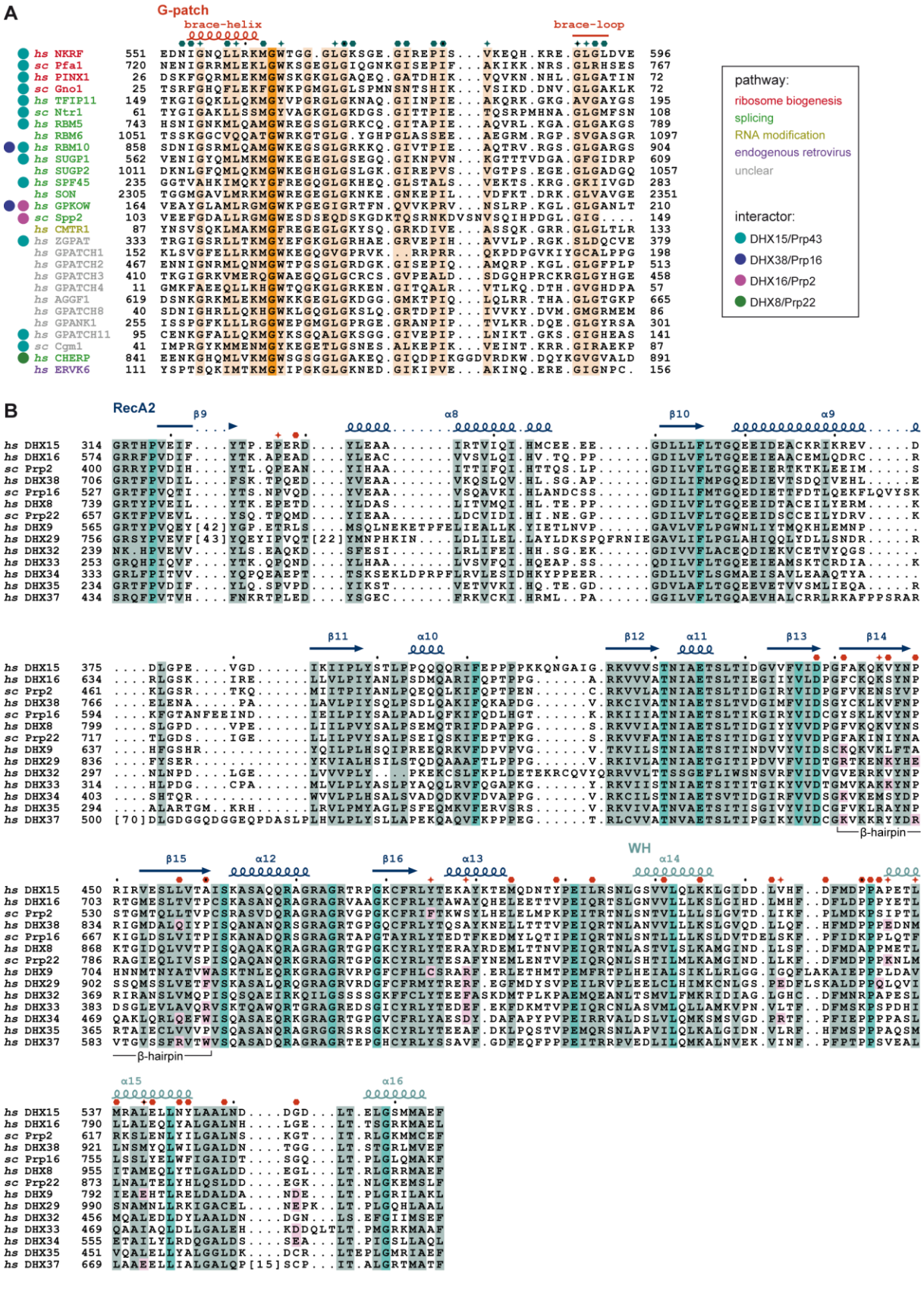

Fig. S2. Conservation of DEAH-G-patch interface residues.

(*A*) Sequence alignment of all known human and yeast G-patch proteins. G-patch residues relevant for helicase binding are well conserved. Coloring and labelling as in Fig. 2*E*. If the proteins have been assigned to a specific pathway, this is indicated by coloring of the protein name. Known (potentially indirectly) interacting DEAH helicases are marked on the side with a colored dot. (*B*) Alignment of human and yeast DEAH helicases. While G-patch binding sites are maintained in DHX15/Prp43 and DHX16/Prp2 orthologs, several other DEAH family members have potentially disruptive substitutions, DHX35 being the only exception. Coloring and labelling as in Fig. S1. Substitutions in G-patch binding pockets that could prevent an interaction as it is observed in the current structure are highlighted in pink.

Studer et al. Supplemental Figure 3

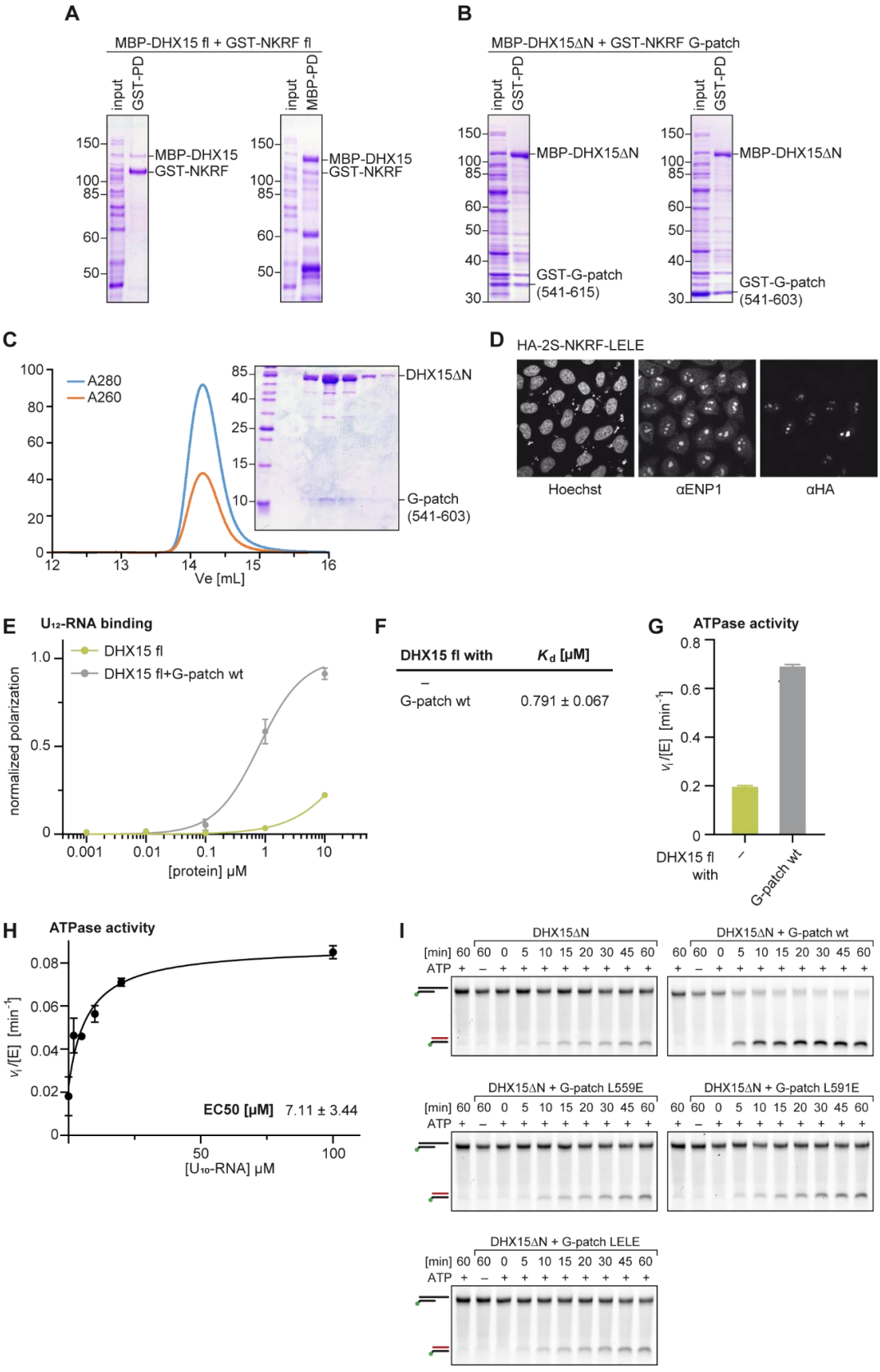

Fig. S3. DHX15 fl and ΔN constructs show similar binding and activation by NKRF G-patch.

(*A*) Coomassie stained protein gels from copurification assays of MBP-DHX15 fl and GST-NKRF fl after coexpression in *E. coli* using glutathione (left) or maltose (right) resin. (*B*) Coomassie stained protein gels from copurification assays of MBP-DHX15ΔN with NKRF G-patch constructs of different lengths after coexpression in *E. coli*. Complexes were enriched on glutathione resin. (*C*) Elution profile of a representative gel filtration run from purification of the DHX15ΔN-G-patch complex. A coomassie stained SDS-gel of the corresponding fractions is shown next to the chromatogram. Due to its small size the G-patch peptide is stained weaker compared to the large DHX15ΔN protein. (*D*) Immunofluorescence of HeLa K cells transfected with HA-2S-NKRF LELE mutant shows its correct localization to nucleoli. Hoechst staining indicates positions of nuclei, while ENP1 detection serves to position nucleoli and cyctoplasm. In all cells expressing HA-2S-NKRF LELE the protein is detected in nucleoli. (*E*) Fluorescence polarization assays for binding of FAM-U_{12} RNA by DHX15 fl with and without GST-G-patch wt. Error bars indicate SD of triplicates. (*F*) Dissociation constants and their SEM extracted by linear regression fitting of fluorescence polarization data shown in *E*. An approximate K_d is given for DHX15 fl, because 0.5 normalized polarization was not reached. (*G*) ATPase activity of DHX15 fl with and without GST-G-patch wt measured by an NADH-dependent continuous coupled-assay. Initial rates at 2 mM ATP were determined in triplicates and normalized for the enzyme concentration. Error bars represent SD. (*H*) RNA concentration dependence of the ATPase activity of DHX15ΔN without G-patch. U_{10} RNA was titrated while the ATP concentration was maintained at 2 mM. Error bars indicate SD of triplicates. The EC50 value and the corresponding SEM were extracted by linear regression. (*I*) Representative native RNA gels that were used to fit time courses of RNA duplex unwinding by DHX15ΔN with or without GST-G-patch wt or mutants. Samples incubated without ATP or without protein served as controls for RNase contamination.

Studer et al. Supplemental Figure 4

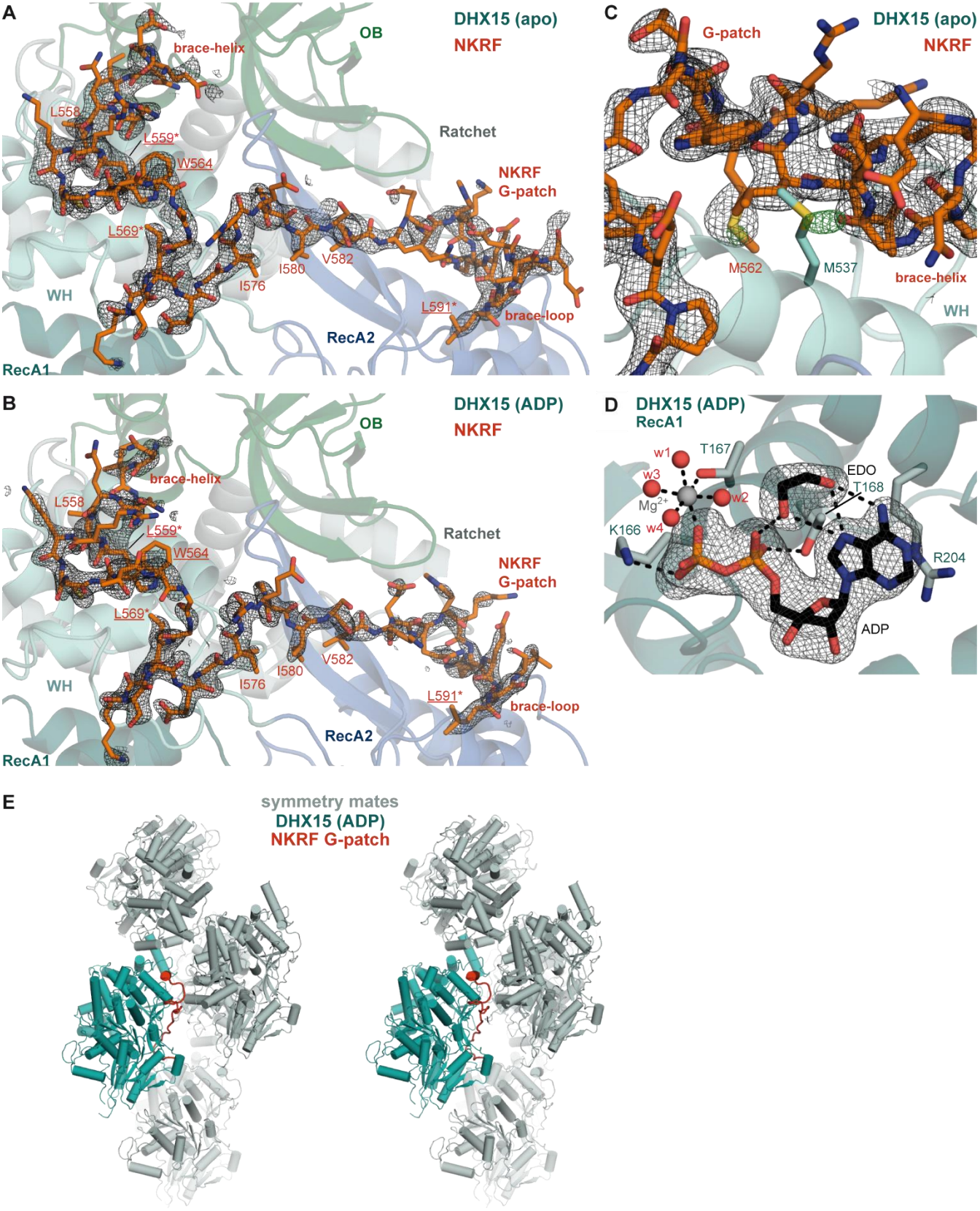

Fig. S4. G-patch peptides and ADP are well ordered in the structures without involvement of crystal contacts.

(*A*, *B*) Omit maps (black) of the entire G-patch motif contoured at 1.0σ in the DHX15Δ-G-patch complex without (*A*) or with (*B*) ADP bound. Positions of several crucial or mutated residues are indicated and labelled as in Fig. 2*B*-*D*. (C) Omit map (black) of the G-patch in the apo structure together with the anomalous difference density of the native S-SAD experiment (green) contoured at 3.3σ zoomed in at NKRF M562 in the brace-helix and DHX15 M537 in the WH. The anomalous density map indicates positions of sulfur atoms in the structure, and was used to verify sequence assignment in the G-patch motif structure. (*D*) Polder map (1) of ADP and ethylene glycol from the crystallization condition in the active site between the two RecA domains of DHX15 next to the catalytic Mg^{2+} ion. The density is contoured at 4.0σ. (*E*) Stereo image of the crystal packing of the DHX15ΔN-G-patch complex in the ADP-bound structure. Packing of the apo structure is analogous. The G-patch peptide is not involved in any crystal contacts (closest side-chain distance >5 Å).

Studer et al. Supplemental Figure 5

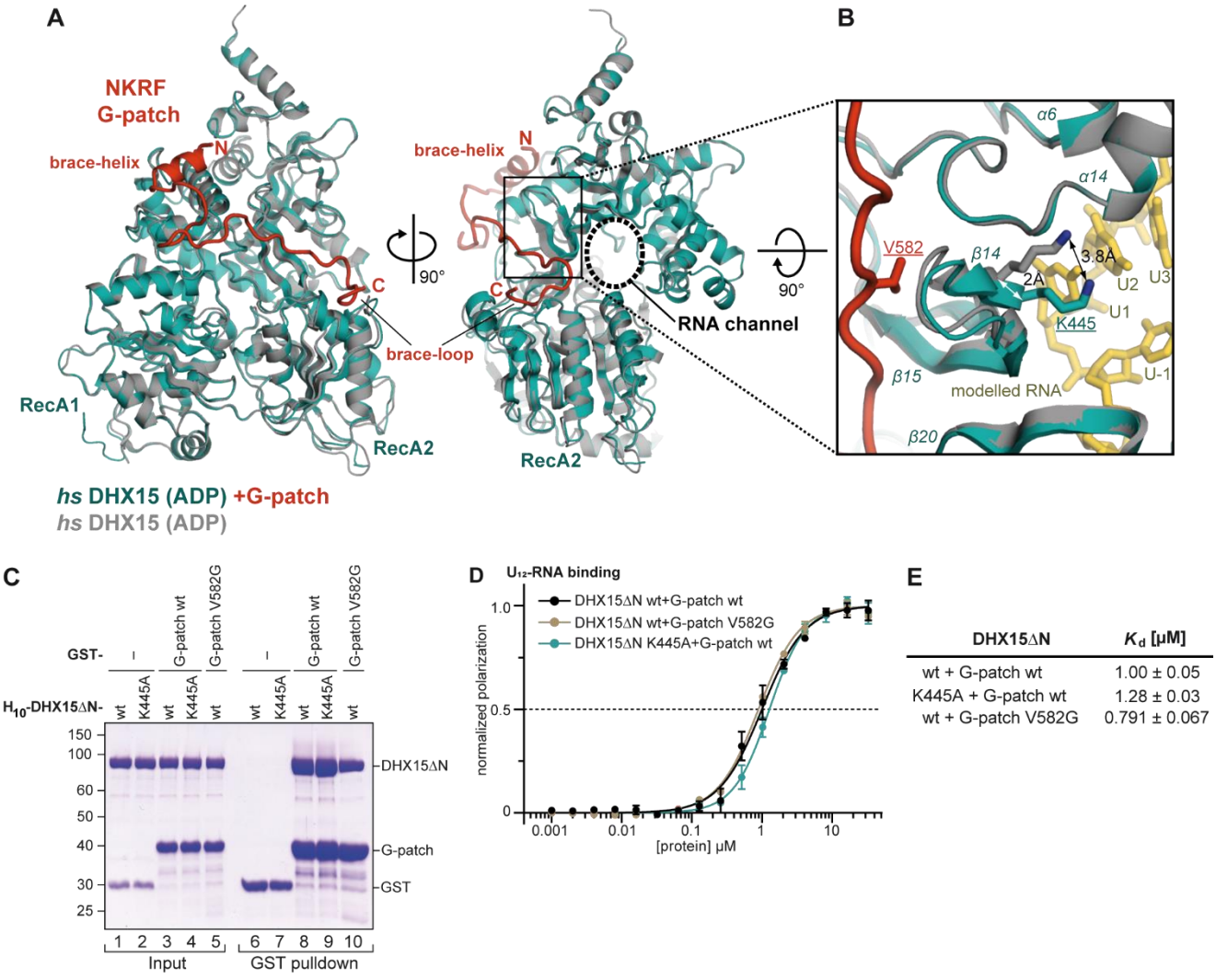

Fig. S5. Effect of G-patch binding on DHX15 β-hairpin.

(*A*) G-patch binding pushes the β-hairpin inwards into the RNA binding channel. Superposition of *hs*DHX15ΔN (ADP) with or without G-patch (PDB ID 5xdr (2)), in petrol/red and grey, respectively. Position of the zoomed view in panel *B* is indicated by a black box. The location of the RNA binding channel is marked by a dashed ellipse. (*B*) Focused view onto the conformational change of the β-hairpin in DHX15. The shift of K445 due to interactions of G-patch V582 with the outside of β14 is indicated. To visualize the potential position of the RNA in the channel, RNA (yellow) from a *ct*Prp43 structure (PDB ID 5lta (3)) is modelled by superposition. The base of U1 is closest to K445. (*C*) Coomassie stained gels of copurification assays of purified His_{10}-DHX15ΔN wt or K445A mutant and GST-NKRF G-patch wt or V582G mutant. GST served as a control. (*D*) Fluorescence polarization assays for binding of FAM-

U_{12} RNA by DHX15ΔN K445A with GST-G-patch wt or DHX15ΔN wt with GST-G-patch V582G mutant. Error bars indicate SD of triplicates. (*F*) Dissociation constants and their SEM extracted by linear regression fitting of fluorescence polarization data shown in *E*.

Studer et al. Supplemental Figure 6

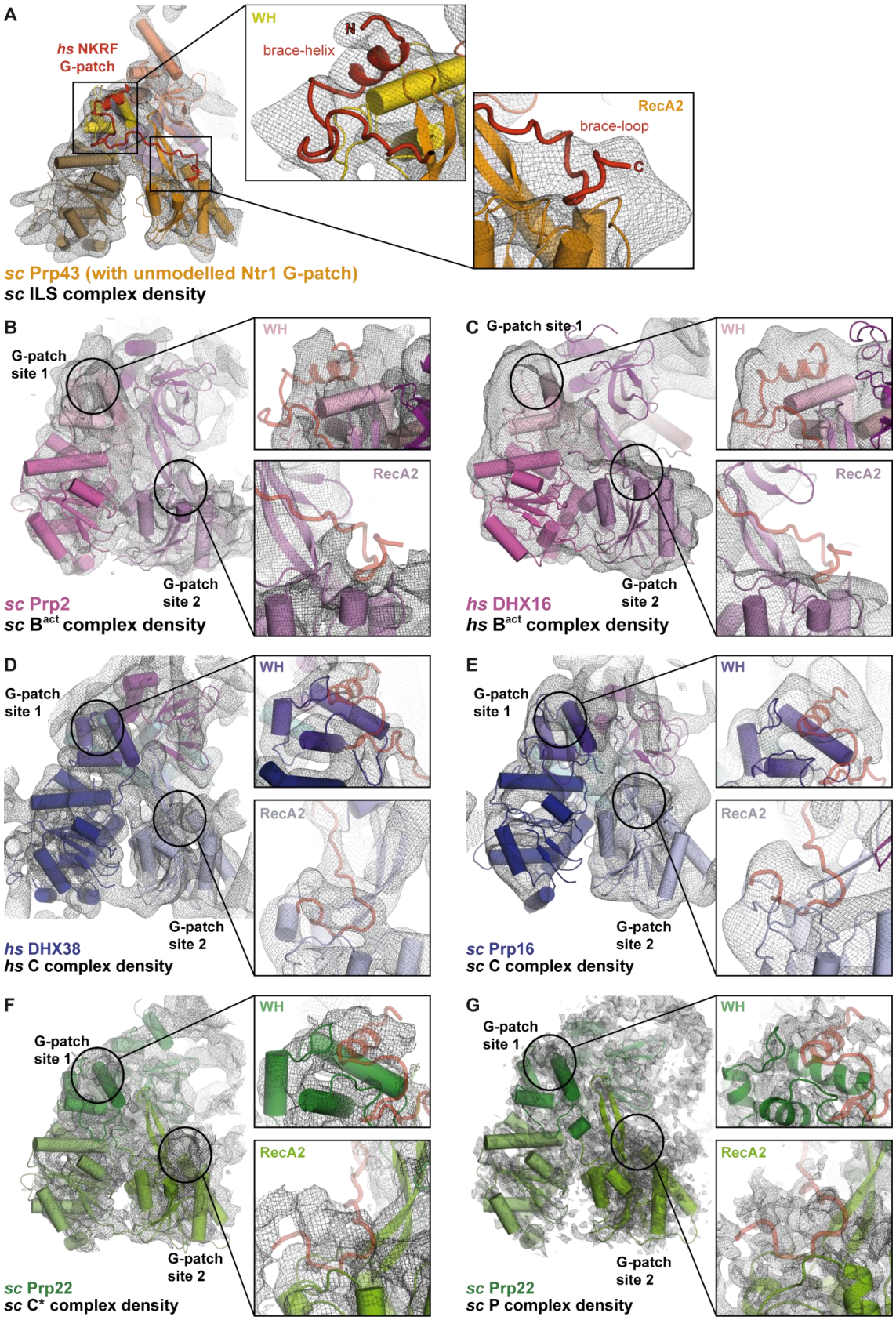

Fig. S6. cryoEM maps of different spliceosomal complexes around the respective DEAH helicases indicates occupation of G-patch sites by unmodelled proteins.

(*A*) *sc*ILS complex map (EMD-6817 additional map 1, PDB ID 5y88) (4) contoured at 1.5σ shows good fit on *sc*Prp43 with the NKRF G-patch peptide both on G-patch site 1 (WH) and site 2 (RecA2). The peptide was placed by superposition of Prp43 from the ILS model with the *hs*DHX15ΔN-G-patch (apo) complex. The *sc*Ntr1 G-patch was present in the ILS complex but not modelled due to low local resolution. (*B*-*G*) CryoEM maps of all other DEAH helicases in all available spliceosomal complexes, that had sufficiently resolved maps around the helicases for inspection. The positions of the G-patch brace-helix and brace-loop are modelled by superposition with the *hs*DHX15-G-patch (apo) structure, and shown as a transparent red cartoon. (*B*) CryoEM map and structure of *sc*Prp2 in the *sc*B^{act} spliceosome contoured at 5.5σ (EMD-4099, PDB ID 5lqw) (5). (*C*) *hs*DHX16 in the *hs*B^{act} complex map contoured at 3.8σ (EMD-4240, PDB ID 6ff7) (6). (*D*) *hs*DHX38 in the *hs*C spliceosome map contoured at 6.5σ (EMD-6864, PDB ID 5yzg) (7). (*E*) *sc*Prp16 in the map of the *sc*C splicing complex after branching contoured at 7.0σ (EMD-4057, PDB ID 5lj5) (8). (*F*) *sc*Prp22 in the map of the *sc*C* spliceosome before exon ligation contoured at 8.0σ (EMD-3541, PDB ID 5mq0) (9). (*G*) *sc*Prp22 in the map of the post-catalytic *sc*P splicing complex contoured at 4.8σ (EMD-7109, PDB ID 6bk8) (10).

Studer et al. Supplemental Figure 7

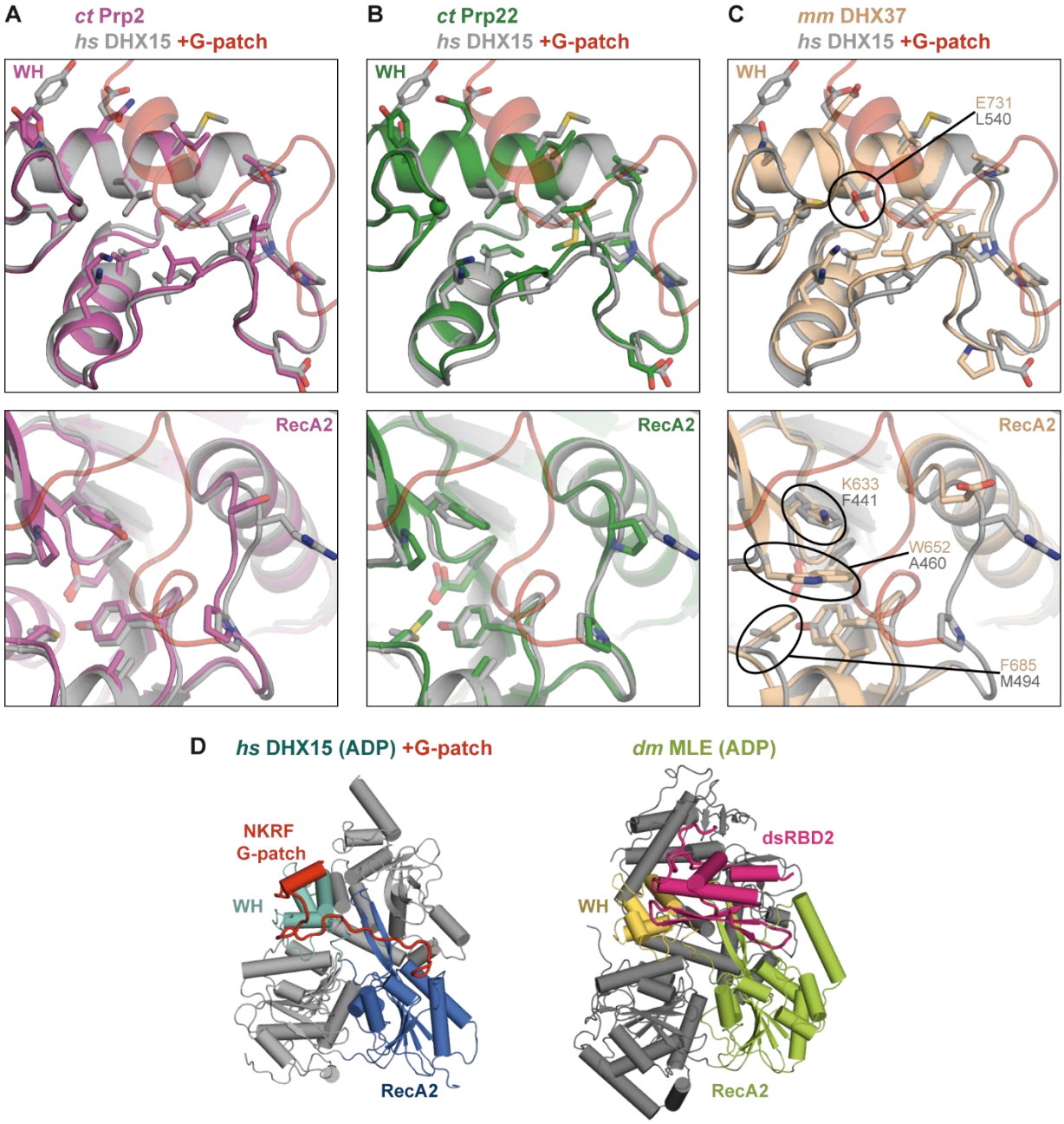

Fig. S7. Comparison of the *hs*DHX15-G-patch complex to other DEAH/RHA helicase structures reveals the basis for G-patch selectivity.

(*A-C*) Superposition of the complex onto both G-patch sites on WH and RecA2 domain from (*A*) *ct*Prp2 (11), (*B*) *ct*Prp22 (12) and (*C*) *mm*DHX37 (13). The G-patch motif is shown as a transparent red cartoon, DHX15 is shown in grey, while the other structures are shown in color. Potentially significant

substitutions in the binding sites are circled and residues labelled. (*D*) Comparison of *hs*DHX15-G-patch to the DEAH/RHA helicase *dm*MLE/DHX9 (14). The analogous placement of dsRBD2 (magenta) that also binds across WH (yellow) and RecA2 (green) is highlighted. The other domains are shown in grey. The orientation of *dm*MLE is analogous to the DHX15 structure on the left.

Table S1. Data collection and refinement statistics

DATA SET	**DHX15 – NKRF G-patch (apo)**	**DHX15 – NKRF G-patch (with ADP)**	**DHX15 – NKRF G-patch (Sulfur SAD)**
Space group	$C222_1$	$C222_1$	$C222_1$
Unit cell			
dimensions (a, b, c) (Å)	82.2, 90.0, 213.9	82.9, 91.2, 212.8	83.2, 92.0, 215.8
angles (α, β, γ) (°)	90, 90, 90	90, 90, 90	90, 90, 90
DATA COLLECTION[a]			
Wavelength	1.000041	0.999999	2.066400
Resolution range, (Å)	46.23-2.21 (2.29-2.21)	46.40-1.85 (1.92-1.85)	46.84-2.80 (2.90-2.80)
R_{meas}, %	18.7 (282)	14.8 (422)	15.4 (109)
R_{pim}, %[b]	5.2 (76.3)	4.0 (113)	2.2 (20.6)
Completeness, %	99.8 (98.7)	99.9 (98.9)	98.6 (97.2)
Mean $I/\sigma(I)$	8.2 (0.7)	13.4 (0.7)	23.3 (2.6)
Unique reflections	39975 (3912)	68754 (6760)	20544 (1980)
Multiplicity	13.1 (13.5)	13.4 (13.6)	44.1 (27.4)
$CC_{1/2}$	99.8 (38.0)	99.9 (38.7)	99.9 (96.3)
Wilson B	46.3	26.7	90.4
REFINEMENT			
Data range, (Å)	46.23-2.21	46.40-1.85	
R_{cryst}, %	20.90	20.35	
R_{free}, %	25.08	24.43	
Number of atoms per asymmetric unit			
all atoms	5745	6159	
protein	5711	5828	
ligand	-	32	
water	34	299	
Average *B*-factor, (Å^2)			
all atoms	79.88	52.24	
protein	79.95	52.41	
ligand	-	48.40	
water	67.42	49.44	
Ramachandran plot			
favored regions, %	96.58	97.21	
disallowed regions, %	0.00	0.00	
Rmsd from ideal geometry			
bond lengths, (Å)	0.002	0.010	
bond angles, (°)	0.472	1.041	
PDB code	6SH7	6SH6	

[a]Values in parentheses are for highest-resolution shell.

[b]R_{pim} gives the precision of averaged intensities and is a better indicator for data quality in highly redundant datasets than R_{merge}, which penalizes redundancy which penalizes redundancy (15).

SI REFERENCES

1. D. Liebschner, *et al.*, Polder maps: improving OMIT maps by excluding bulk solvent. *Acta Crystallogr D Biol Crystallogr* **73**, 148–157 (2017).

2. K. Murakami, K. Nakano, T. Shimizu, U. Ohto, The crystal structure of human DEAH-box RNA helicase 15 reveals a domain organization of the mammalian DEAH/RHA family. *Acta Crystallogr F Struct Biol Commun* **73**, 347–355 (2017).

3. M. J. Tauchert, J.-B. Fourmann, R. Lührmann, R. Ficner, Structural insights into the mechanism of the DEAH-box RNA helicase Prp43. *eLife* **6** (2017) doi:10.7554/eLife.21510.

4. R. Wan, C. Yan, R. Bai, J. Lei, Y. Shi, Structure of an Intron Lariat Spliceosome from Saccharomyces cerevisiae. *Cell* **171**, 120-132.e12 (2017).

5. R. Rauhut, *et al.*, Molecular architecture of the Saccharomyces cerevisiae activated spliceosome. *Science* **353**, 1399–1405 (2016).

6. D. Haselbach, *et al.*, Structure and Conformational Dynamics of the Human Spliceosomal Bact Complex. *Cell* **172**, 454-464.e11 (2018).

7. X. Zhan, C. Yan, X. Zhang, J. Lei, Y. Shi, Structure of a human catalytic step I spliceosome. *Science* **359**, 537–545 (2018).

8. W. P. Galej, *et al.*, Cryo-EM structure of the spliceosome immediately after branching. *Nature* **537**, 197–201 (2016).

9. S. M. Fica, *et al.*, Structure of a spliceosome remodelled for exon ligation. *Nature* **542**, 377–380 (2017).

10. S. Liu, *et al.*, Structure of the yeast spliceosomal postcatalytic P complex. *Science* **358**, 1278–1283 (2017).

11. A. Schmitt, F. Hamann, P. Neumann, R. Ficner, Crystal structure of the spliceosomal DEAH-box ATPase Prp2. *Acta Crystallogr D Struct Biol* **74**, 643–654 (2018).

12. F. Hamann, M. Enders, R. Ficner, Structural basis for RNA translocation by DEAH-box ATPases. *Nucleic Acids Res* **47**, 4349–4362 (2019).

13. F. M. Boneberg, *et al.*, Molecular mechanism of the RNA helicase DHX37 and its activation by UTP14A in ribosome biogenesis. *RNA* **25**, 685–701 (2019).

14. J. R. Prabu, *et al.*, Structure of the RNA Helicase MLE Reveals the Molecular Mechanisms for Uridine Specificity and RNA-ATP Coupling. *Mol Cell* **60**, 487–499 (2015).

15. M. S. Weiss, Global indicators of X-ray data quality. *J Appl Cryst* **34**, 130–135 (2001).